Geochemistry
Geophysics
Geosystems
G3
AN ELECTRONIC JOURNAL OF THE EARTH SCIENCES
Published by AGU and the Geochemical Society

Article
Volume 9, Number 10
21 October 2008
Q10T03, doi:10.1029/2008GC002128
ISSN: 1525-2027

Click Here for Full Article

Frequency-magnitude distribution of microearthquakes beneath the 9°50′N region of the East Pacific Rise, October 2003 through April 2004

D. R. Bohnenstiehl

Department of Marine, Earth and Atmospheric Sciences, North Carolina State University, Campus Box 8208, Raleigh, North Carolina 27695, USA (drbohnen@ncsu.edu)

F. Waldhauser and M. Tolstoy

Lamont-Doherty Earth Observatory of Columbia University, P.O. Box 1000, Palisades, New York 10964, USA

[1] Relocated hypocentral data from a 7-month deployment (October 2003 to April 2004) of ocean bottom seismometers provide an opportunity to map microearthquake frequency-magnitude distributions (FMDs) along the 9°49–52′N region on the East Pacific Rise. These analyses, which incorporate more than 9000 earthquakes, represent the first investigation of the 3-D spatial and temporal patterns of FMDs along any mid-ocean ridge spreading center. The data are described well by a Gutenberg-Richter model, indicating a power law or fractal relationship between earthquake size and frequency. The scaling exponent, or *b* value, shows significant spatial variability, exceeding a value of 2.0 at the shallowest depths on axis and dropping below 1.0 away from the axial trough. This spatial pattern is consistent with an inverse relationship between *b* value and ambient stress conditions, with the lowest stress levels at shallow depths and relatively high stress levels (or low pore pressures) observed away from the axial zone. Intermediate *b* values are observed on-axis above the ridge system's melt lens; however, within this region there also exists significant spatial variability. This indicates that stress conditions and/or structural heterogeneity may vary at subkilometer scales within the hydrothermal circulation cell. Although the observational period is characterized by increasing seismicity rates, building toward an eruptive episode in January 2006, the first-order spatial pattern of *b* values is sustained, with no overall temporal trend. As a byproduct of this *b* value analysis, the detection capabilities of the array are assessed empirically.

Components: 9916 words, 11 figures, 3 tables.

Keywords: *b* values; microearthquakes; hydrothermal circulation; East Pacific Rise; mid-ocean ridge seismicity.

Index Terms: 3035 Marine Geology and Geophysics: Midocean ridge processes; 3017 Marine Geology and Geophysics: Hydrothermal systems (0450, 1034, 3616, 4832, 8135, 8424); 7245 Seismology: Mid-ocean ridges.

Received 15 June 2008; **Revised** 21 August 2008; **Accepted** 28 August 2008; **Published** 21 October 2008.

Bohnenstiehl, D. R., F. Waldhauser, and M. Tolstoy (2008), Frequency-magnitude distribution of microearthquakes beneath the 9°50′N region of the East Pacific Rise, October 2003 through April 2004, *Geochem. Geophys. Geosyst.*, *9*, Q10T03, doi:10.1029/2008GC002128.

Theme: Recent Volcanic Eruptions, Properties, and Behavior of the Fast Spreading East Pacific Rise at 8°–11°N
Guest Editors: S. Carbotte, R. Haymon, and B. Seyfreid

1. Introduction

[2] The power law size-frequency distribution of earthquakes is often referred to as the *Gutenberg and Richter* [1944] relationship:

$$\log_{10}(N) = a - bM, \tag{1}$$

where M is earthquake magnitude (a logarithmic measure of earthquake size), N is the cumulative number of earthquakes $\geq M$, and a and b are empirical constants. The a value describes the seismic productivity of an area and the b value describes the relative proportion of small and large magnitude events (i.e., the distribution's slope on a plot of log (N) versus M).

[3] The *b* value is among the most widely reported statistics in seismology. Although its globally averaged value is approximately 1 [e.g., *Frohlich and Davis*, 1993], *b* values may vary by as much as a factor of three at both local and regional scales [*Wiemer and Wyss*, 2002]. The parameters influencing *b* value remain somewhat enigmatic; however, laboratory and numerical models indicated that the parameter scales inversely with ambient stress conditions [e.g., *Scholz*, 1968; *Amitrano*, 2003]. This is supported by a growing number of field observations, including: (1) studies that show decreases in *b* value accompany increases in stress release preceding rock burst events in underground mines [e.g., *Urbancic et al.*, 1992; *Nuannin et al.*, 2002, 2005], (2) the correlation of high pore pressures (low-effected stress) with high *b* value [e.g., *Wyss*, 1973; *Wiemer et al.*, 1998], (3) the mapping of low *b* value in regions of known asperities along the San Andreas fault [*Wiemer and Wyss*, 1997], and (4) the correlation between *b* value and focal mechanism, with decreasing *b* value associated with the increasing stress levels characteristic of normal, strike-slip, and thrust environments [*Schorlemmer et al.*, 2005]. Conceptually, the dependence of *b* value on stress implies that small ruptures are more likely to grow into large earthquakes in high-stress areas, since the system contains more energy and the rupture can more easily connect across subvolumes with lower stress concentrations [*Scholz*, 1968]. Alternatively, *b* value patterns may reflect variability in the distribution of fractures within a rock volume [e.g., *Barton et al.*, 1999; *Henderson et al.*, 1999; *Wyss et al.*, 2004], whereby higher *b* values (a greater proportion of small earthquakes) indicate greater structural heterogeneity [*Mogi*, 1962]. Experimental evidence also suggests that increasing thermal gradients or heterogeneous stress conditions generated by nonuniform temperature distributions may result in higher *b* values [*Warren and Latham*, 1970].

[4] Power law size-frequency distributions previously have been noted in mid-ocean ridge (MOR) settings from the analysis of global seismic catalogs [e.g., *Francis*, 1968], regional hydroacoustic recordings [*Fox et al.*, 1994; *Bohnenstiehl et al.*, 2002, 2004], and local ocean bottom seismometer (OBS) data (Table 1). Estimates of MOR *b* value from global earthquake catalogs are primarily limited to slow spreading environments, where the near-axis lithosphere is of sufficient thickness to generate earthquakes that can be detected consistently by land-based seismic stations (M > 4.5). However, owing to low data density along the ridge, studies typically require averaging across large temporal and spatial scales. This not only limits the resolution of the analysis but also may result in the mixing of distinct earthquake populations [*Kagan*, 2002; *Bird et al.*, 2002].

[5] A more complete record of MOR earthquakes ($M > \sim3$) may be provided by regional hydrophone arrays, which locate seismically generated acoustic phases, known as tertiary (T) waves [e.g., *Fox et al.*, 1994, 2001]. In these studies, the size of an earthquake is represented in terms of its acoustic source level (dB re 1 μPa @ 1m). Source level-frequency distributions also exhibit a power law behavior and have been used to show temporal changes in the relative proportions of small and large earthquakes when seismic activity is colocated [e.g., *Bohnenstiehl et al.*, 2004]. However, scatter in the source level-magnitude relationship typically prevents a robust comparison with seismic-based *b* value estimates, and the potential dependence of T wave amplitude on local seafloor morphology may make it difficult to map and compare changes in *b* value between distant regions.

[6] Survey parameters from OBS studies reporting *b* values in the MOR environment are given in Table 1. These autonomous instruments extend the monitoring range to microearthquake levels (M < 2), but most OBS deployments have been of limited duration due to power and data storage constraints in previous decades. Published *b* value estimates are found only for slow-to-intermediate spreading rate ridges (20–60 mm/a), where most passive microseismic OBS experiments have been focused.

Table 1. Summary of Ocean Bottom Seismometer-Based *b* Value Studies in a Mid-Ocean Ridge Setting[a]

Reference	Location	Description	M_c	M_{max}	N	N (M_c)	Number of Days	*b* Value
1	MAR 5°S	valley floor	1.6	2.7	80	40	10	1.27 ± 0.14
2[b]	MAR 23°N	valley floor	1.5	2.4	20	10	10	1.2 ± 0.1[c]
2[b]	MAR 23°N	valley walls	1.5	2.4	20	20	10	0.75 ± 0.1[c]
3[b]	MAR 26°N	TAG segment (all)	2.0	3.0	136	70	23	1.5 ± 0.1[c]
3[b]	MAR 26°N	TAG segment center	2.0	3.0	–	25	23	1.65–2.25 ± 0.1[c]
3[b]	MAR 26°N	TAG segment end	2.0	3.0	–	25	23	0.9–1.3 ± 0.1[c]
4[b]	MAR 29°N	inside corner/axial valley	–	2.7	1000	–	41	0.82 ± 0.05[c]
5	MAR 35°N	segment center	1.0	2.3	100	50	43	1.41 ± 0.05[c]
6	MAR 35°N	segment end/transform	0.2	2.0	120	55	12	0.75–1.05[c]
7	MAR 45°N	swarm-like	1.8	3.5	200	90	6	1.05
7	MAR 45°N	aftershock-like	2.8	4.6	200	70	6	1.04
8	JdFR 48.5°N	dead dog vent	–	0.2	480	–	142	1.49
9	JdFR 48°N	end segment (all)	1.0	2.7	1750	700	55	1.41[c]
9	JdFR 48°N	axial region	1.0	2.7	700	400	55	1.5[c]
9	JdFR 48°N	proximal	1.0	2.7	1050	500	55	1.59[c]
10	RTJ	RTJ (all)	2.8	4.0	220	85	21	1.31
10	RTJ	SEIR	2.8	3.9	85	41	21	1.46
10	RTJ	SWIR	2.8	3.7	60	30	21	1.1

[a] References: 1, *Tilmann et al.* [2004]; 2, *Toomey et al.* [1988]; 3, *Kong et al.* [1992]; 4, *Wolfe et al.* [1995]; 5, *Barclay et al.* [2001]; 6, *Cessaro and Hussong* [1986]; 7, *Lilwall et al.* [1977]; 8, *Golden et al.* [2003]; 9, *Wilcock et al.* [2002]; 10, *Katsumata et al.* [2001]. When not specified by the authors, parameters have been estimated from frequency-magnitude distribution plots. Long dashes indicate parameters that could not be determined. M_c is magnitude of completeness; M_{max} is maximum magnitude; N_{tot} is total number of earthquakes; $N(M_c)$ is number of earthquake $\geq M_c$. MAR is Mid-Atlantic Ridge; JdFR is Juan de Fuca Ridge; RTJ is Rodriguez Triple Junction; SEIR is Southeast Indian Ridge; SWIR is Southwest Indian Ridge. TAG is Trans-Atlantic Geotraverse.

[b] Some or all of the ocean bottom seismometers recorded in event-detection or trigger mode. Other deployments used continuously recording stations.

[c] β value or exponent of moment-frequency distribution is cited by the authors. Values have been convert to a magnitude-frequency *b* value assuming $M \propto 2/3*\log_{10}(M_o)$ or $b = 3/2\beta$ scaling [*Scholz*, 2002].

[7] This study describes the size-frequency distributions of microearthquakes in the vicinity of the 9°50′N vent field of the East Pacific Rise (EPR, 110 mm/a), a site of long-term and interdisciplinary study coordinated by the RIDGE 2000 initiative (Figure 1). The data set, which spans the time period between October 2003 and April 2004 and contains more than 9000 accurately located events, represents one of the most extensive and the longest duration microseismic catalogs published within an oceanic spreading environment [*Tolstoy et al.*, 2006, 2008]. We utilize these data to examine, for the first time, the 3-D spatial and temporal patterns in the frequency-magnitude distribution (FMD) of ridge-crest earthquakes.

[8] The various instrumentation, processing procedures, and definitions of earthquake size used in previous OBS studies (Table 1) may result in magnitude scales that are compressed or stretched relative to one another, resulting in systematic differences in the absolute value of the *b* parameter.

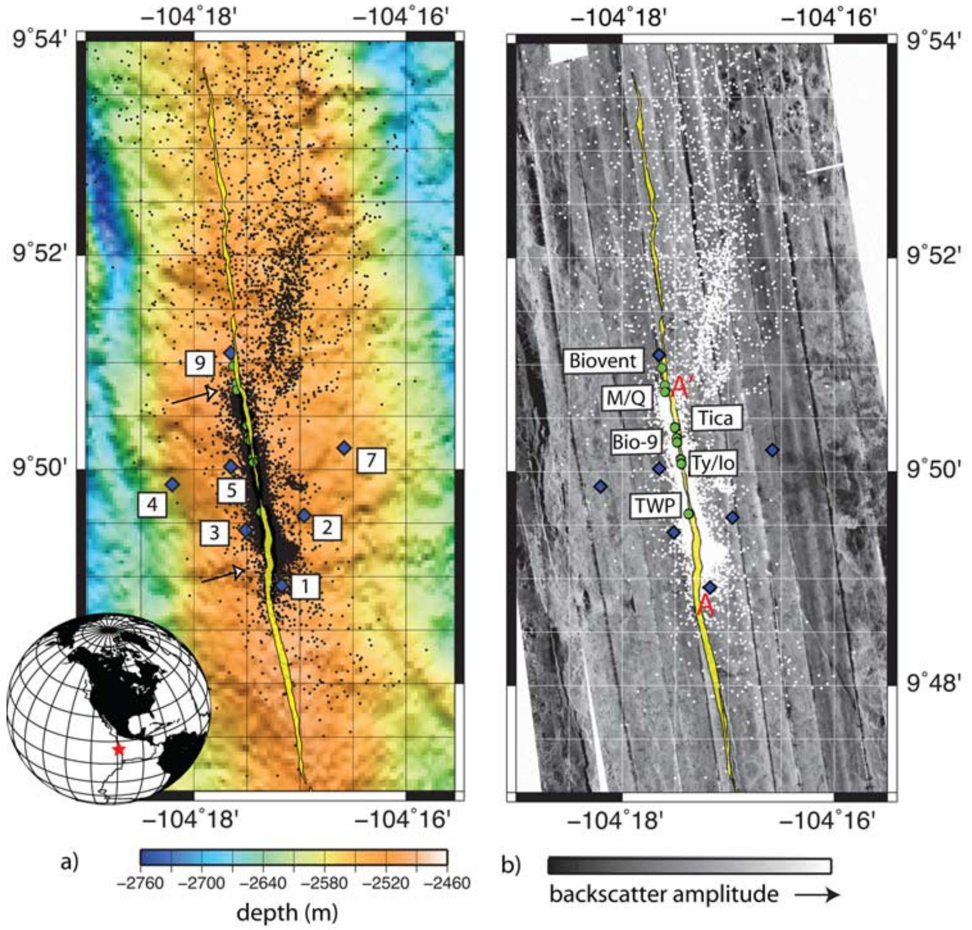

Figure 1. Location map showing microearthquake epicenters (dots) overlying (a) multibeam bathymetric data (http://www.marine-geo.org/) [*White et al.*, 2006] and (b) side scan sonar imagery collected using the deeply towed DSL-120 system [*Fornari et al.*, 2004]. Yellow shading outlines the location of the axial summit trough (AST) prior to the 2006 eruption [*Fornari et al.*, 2004; *Soule et al.*, 2005; *Escartin et al.*, 2007]. Blue diamonds indicate the locations of ocean bottom seismometer (OBS)/ocean bottom hydrophone instruments used to locate events; green circles mark the locations of many of the well-studied, high-temperature vents systems in the area; white arrows identify small axial discontinuities; cross sections shown in Figures 2 and 5 are along the line A-A′. Inset shows global location of study area.

Similar conditions are well documented among terrestrial networks [e.g., *Wyss and Toya*, 2000; *Oncel and Wyss*, 2000; *Westerhaus et al.*, 2002]. However, when a consistent magnitude scale is applied within a given region, differences in *b* value can be defined reliably [*Wiemer and Wyss*, 2002]. This allows us to focus on local changes in the *b* value as a function of space and time and relate the observed patterns to changing stress conditions or fracture characteristics within the crust [e.g., *Wiemer et al.*, 1998; *Wyss et al.*, 2004].

[9] As a byproduct of the *b* value analysis, an assessment of the detection capabilities of the OBS network is produced. This is expressed in terms of the magnitude of completeness (M_c), defined as the smallest magnitude that is consistently represented within the earthquake catalog. Accounting for temporal and spatial variability in an OBS array's detection capabilities may be necessary in some statistical applications, and this information should be considered as the community uses these data.

2. Ocean-Bottom Seismic Experiment

[10] From October 2003 to April 2004, seven autonomous seafloor stations were instrumented with vertical-channel short-period seismometers (L22 Mark Products) and omnidirectional hydrophones (Figure 1). *P* wave detections were generated using a STA-LTA algorithm implemented within the Antelope Processing Suite and operating

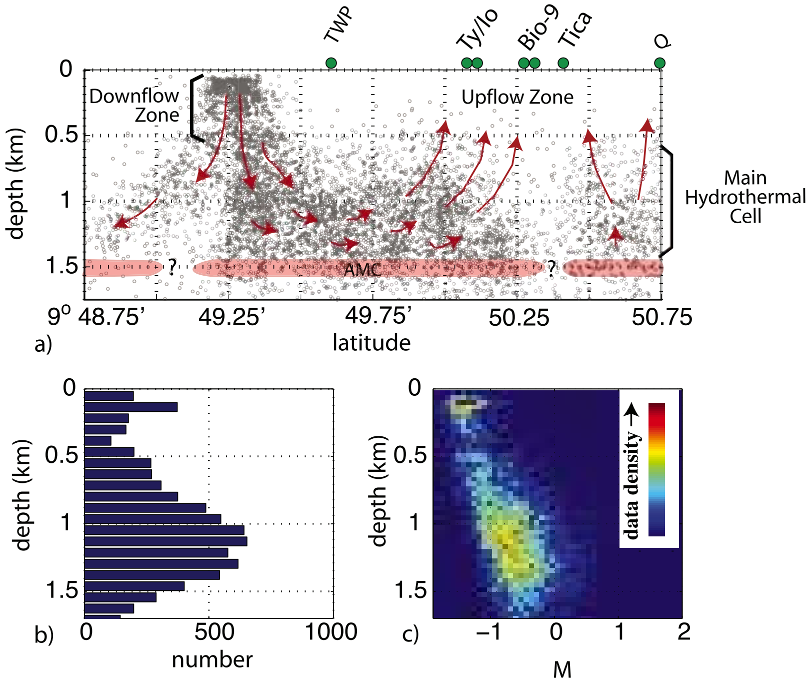

Figure 2. (a) Axial cross section of seismicity along A-A′ (Figure 1); interpretation following *Tolstoy et al.* [2008]. The axial magma chamber (AMC) is sketched at the seismically determined depth reported by *Kent et al.* [1993]. (b) Histogram showing depth distribution of earthquakes within the array. (c) Magnitude versus depth density plot for events within the array.

in the 14–25 Hz frequency band. These detections were automatically associated to form events and subsequently reviewed by an analyst, who made adjustments and manually added *S* wave arrivals.

[11] Analyst-reviewed arrivals from a well-recorded subset of events were used to invert for the best fitting 1-D local velocity model using the *Velest* algorithm [*Kissling et al.*, 1994]. Absolute locations were derived by minimizing the weighted squares of the residuals between the 1-D predicted and observed traveltimes using *Hypoinverse* [*Klein*, 2002]. In an effort to remove remaining model errors in the Hypoinverse locations, the double-difference algorithm *hypoDD* [*Waldhauser and Ellsworth*, 2000; *Waldhauser*, 2001] was applied to the *P* and *S* phase data. The *hypoDD* procedure iteratively solves for hypocentral separations by minimizing the residuals between observed and predicted travel time differences for pairs of earthquakes observed at common stations. Within the array, the root-mean-square of the differential time residual decreases by about 91% from 0.125 s before to 0.010 s after relocation. The average difference between *Hypoinverse* and *hypoDD* locations is 270 m. A bootstrap assessment of the relative locations indicates mean errors of 50 m within the array [*Tolstoy et al.*, 2008].

[12] A local magnitude (M_L) scale is derived using the peak displacement amplitude of the vertical-channel seismometer. Following the formulation originated by *Richter* [1935, 1958], local magnitude is defined as:

$$M_L = \log_{10}A - \log_{10}A_o - S, \qquad (2)$$

where A is the peak displacement of the largest arriving phase, $\log_{10}A_o$ is a distance-dependent attenuation correction, and S is a station correction term. The attenuation and station correction terms are inverted for simultaneously using the procedures outlined in Appendix A.

3. Microearthquake Patterns and Geology

[13] The EPR near 9°50′N is a fast spreading mid-ocean ridge system characterized by an axial high morphology and a 50–200 m wide, 5–20 m deep Axial Summit Trough (AST) [*Haymon et al.*, 1991; *Fornari et al.*, 1998]. In 1991, the immediate aftermath of a seafloor eruption was discovered during a series of Alvin dives to the region [*Haymon et al.*, 1993]. Recognizing an opportunity to explore the geological and biological evolution of the site

posteruption, researchers initiated a series of long-term studies focused on the axial hydrothermal systems (Figure 2). In January of 2006, following nearly 15 years of quiescence, this section of the ridge crest erupted again [*Tolstoy et al.*, 2006].

[14] The axial magma chamber (AMC) feeding these eruptions was last imaged during a 1985 multichannel seismic (MCS) survey. Analysis by *Kent et al.* [1993] showed a reflection from the top of the chamber positioned at a depth of ~1.4 km beneath the seafloor, with a thin melt lens having an across-axis width of <500 m. Although these observations were made 2 decades before this study, fast spreading AMCs are long-lived features. Moreover, where axial melt bodies have been imaged using MCS methods, their depth and width commonly show only a few hundred meters of variability at a given spreading rate [*Carbotte*, 2001].

[15] Like other fast spreading ridges, the equatorial EPR appears largely aseismic to global seismic and regional hydrophone arrays, with typically only a small number of $M > 3$ earthquakes observed during suspected volcanic/magmatic episodes [e.g., *Fox et al.*, 2001; *Bohnenstiehl and Dziak*, 2008]. OBS studies, however, indicate more ubiquitous microseismic activity, driven by a combination of thermal, magmatic, and tectonic processes operating near the axis [e.g., *Sohn et al.*, 1998, 1999; *Tolstoy et al.*, 2006, 2008].

[16] The spatial pattern of seismicity shown in Figures 1 and 2 is maintained in a steady state fashion throughout the observational period, October 2003 to April 2004, with minimal swarm activity [*Stroup et al.*, 2007; *Tolstoy et al.*, 2008]. Within the array, hypocenters are concentrated within a 200–300 m wide zone trending along the axis, directly beneath the AST. This corresponds to the region where eruptive activity occurred in 1991 [*Haymon et al.*, 1993] and again in 2006 [*Tolstoy et al.*, 2006; *Soule et al.*, 2007]. In an along-axis cross section (Figures 2a), high hypocentral densities delineate a ~500 m tall zone representing the axial hydrothermal reservoir [*Tolstoy et al.*, 2008]. Seismicity levels begin to decrease approaching the approximate depth of the AMC, reflecting a transition to semibrittle behavior as temperatures approach the brittle-plastic transition (~600°C) for a diabase within the shallow crust (Figure 2) [e.g., *Mackwell et al.*, 1998].

[17] At shallow depths a pipe-like zone of microearthquake activity is observed near 9°49.25′N, coincident with a right-stepping offset of ~100 m in the AST (Figures 1 and 2). This offset has been identified as the B1/B2 segment boundary by *Haymon et al.* [1991]. Given the historic lack of hydrothermal venting and macrofaunal communities near this location [*Haymon et al.*, 1991, 1993; *Shank et al.*, 1998] and long-term trends in vent temperatures [*Scheirer et al.*, 2006], *Tolstoy et al.* [2008] suggested that this pipe-like structure may represent an on-axis downflow zone, where cold seawater is being entrained into the crust. This is in keeping with the idea that segment offsets may represent regions of enhanced crack density [*Haymon et al.*, 1991; *Haymon*, 1996; *Wright et al.*, 1995]. A less-defined zone of shallow seismicity is observed beneath the high-temperature vents at 9°50′N (Figure 2). The apparent absence of seismicity at the shallowest depths in this region may in part reflect the geometry of the seismic array [*Tolstoy et al.*, 2008].

[18] Outside of the array, microearthquakes are located primarily in a north-northeast trending band (Figure 1), the origin of which remains open to debate. During the 2006 eruption, lava was emplaced preferentially on the east rim of the axis, with evidence of off-axis (~600 m east) fissuring and eruption slightly to the north, 9°52–56′N [*Soule et al.*, 2007]. Yet, existing observations do not indicate that this seismically defined lineament served as a magma conduit. A long-term increase in seismicity rate is recorded both within and to the north of the array (Figure 3). This suggests that changes in stressing rate, which control the background rate of seismicity [*Dieterich et al.*, 2000], are coupled between the two zones. Automated event counts from subsequent OBS deployments indicate that the overall rate of seismicity continues to increase, building toward an eruption in January 2006 [*Tolstoy et al.*, 2006].

4. Magnitude of Completeness and *b* Value Analysis

[19] A maximum likelihood estimate of the *b* value is obtained following *Aki* [1965]:

$$b = \frac{\log_{10} e}{\bar{M} - M_c}, \tag{3}$$

where M_c is the cutoff magnitude above which the data set can be considered complete and $\bar{M}$ is the mean magnitude of earthquakes with $M \geq M_c$.

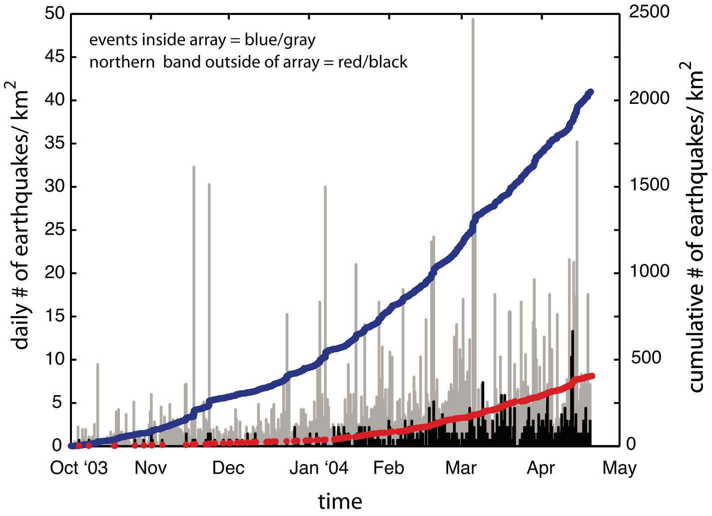

Figure 3. Histogram of daily seismicity rates and cumulative event number during the period October 2003 through April 2004. Earthquakes within the array are shown in blue and gray; Earthquakes within the north-northeast trending band outside of the array (~9°51–52′N) are shown in red and black. Data are normalized per km^2.

[20] Estimates of M_c and b are obtained simultaneously using the procedure outlined by *Wiemer and Wyss* [2000]. Briefly, the b values (equation (1)) are estimated assuming a range of cutoff magnitudes, $M_c = M_i$. For each value of M_i, the goodness-of-fit is computed between the observed FMD and a synthetic population predicted from the maximum likelihood solution. The fit is quantified in terms of the residual error for each cutoff magnitude, given by:

$$R_{M_i} = 100 - \left(\frac{\sum_{M_i}^{M_{\max}} |O_i - S_i|}{\sum_{M_i}^{M_{\max}} O_i} \right) 100, \qquad (4)$$

where O_i and S_i are the number of earthquakes in each cumulative frequency bin for the observed and synthetic populations, respectively. The final value of M_c is selected when R first falls below a threshold value of 10% [e.g., *Wiemer and Wyss*, 2000].

[21] To investigate the b value and M_c patterns as a function of space and time, this procedure is repeated for N size sets of earthquakes. Using a constant number of earthquakes, rather than taking events within a fixed spatial or temporal volume, minimizes the impact of sample size on our estimates. Grid nodes are masked out if they have low hypocentral density or the residual misfit to the power law model is large ($R > 10\%$). The range across which the data are fit is typically ≥ 1.0 magnitude units, although more limited ranges (≥ 0.7 magnitude units) were allowed in the analysis and occur primarily at shallow depths where the maximum magnitude is small and b value is high.

[22] An estimate of the standard deviation in the b value estimate is obtained following *Shi and Bolt*'s [1982] modification of *Aki* [1965]:

$$\delta b = 2.3 b^2 \sqrt{\frac{\sum_i^N (M_i - \bar{M})^2}{n(n-1)}} \qquad (5)$$

where n is sample size. The probability (p) that two samples are drawn from the same population is estimated using the procedure outlined by *Utsu* [1992], which explicitly accounts for the number of events in the sample sets:

$$p \approx \exp\left(\frac{dA}{2} - 2 \right), \qquad (6)$$

where $dA = -2N \ln(N) + 2N_1 \ln(N_1 + N_2 b_1/b_2) + 2N_2 \ln(N_1 b_2/b_1 + N_2) - 2$ and $N = N_1 + N_2$.

5. Results and Observations

5.1. Spatial Patterns

[23] Figure 4 shows the depth distribution of the b and M_c values for all events within the array. This 1-D averaged b value approaches 2.5 at the shallowest depths (<0.3 km) and drops to a value of roughly 1.4 within the hydrothermal cell overlay-

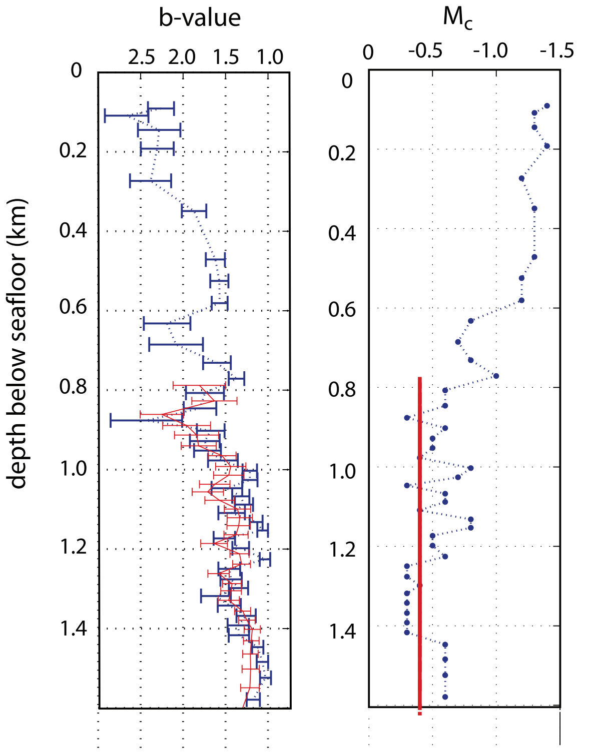

Figure 4. Depth distribution of (a) *b* values and (b) M_c values determined for earthquakes within the array. The *b* value shown by the blue dashed line represents the selection of M_c based on the goodness-of-fit to a power law frequency-magnitude distribution (FMD). The solid red line indicates the *b* value determined using a fixed M_c value of −0.4.

ing the AMC, becoming less variable within the depth range of 0.9–1.4 km. The magnitude of completeness, mapped using the goodness-of-fit procedure outlined in section 4, increases from approximately −1.3 M_L within the shallow pipe to levels of −0.6 to −0.3 above the AMC. To investigate the influence of the M_c selection, the *b* value within the deeper portion of the hydrothermal cell also is mapped using a conservative M_c value fixed at −0.4 (Figure 4). The two *b* value estimates agree well, demonstrating the observed pattern is not dependent on the choice of M_c to within a few magnitude bins ($\Delta M_i = 0.1$ is used in searching for M_c).

[24] When mapped onto an along-axis cross section, the highest *b* values correlate with microearthquakes within the shallow downflow zone. Within the deeper hydrothermal cell, additional heterogeneity is observed with alternating packets of high and low *b* value (Figure 5a). Figure 6 shows the cumulative FMD of events within selected subregions. Hypocenters are selected using a constant volume search, as opposed to mapping a fixed number of events, as in Figures 4 and 5. Utsu's test indicates that the *b* value differences are highly significant between the alternating high and low regions within the hydrothermal cell, and that the *b* values within the shallow downflow zone are significantly higher than elsewhere within the array (Table 2).

[25] Where the accuracy of the hypocentral locations depends strongly on the event magnitude, with small (or large) magnitude events being systematically mislocated into or out of a given volume, a bias may be introduced in the spatial *b* value pattern. In the case of the shallow downflow zone, where the smallest magnitude earthquakes and highest *b* values are detected, travel time

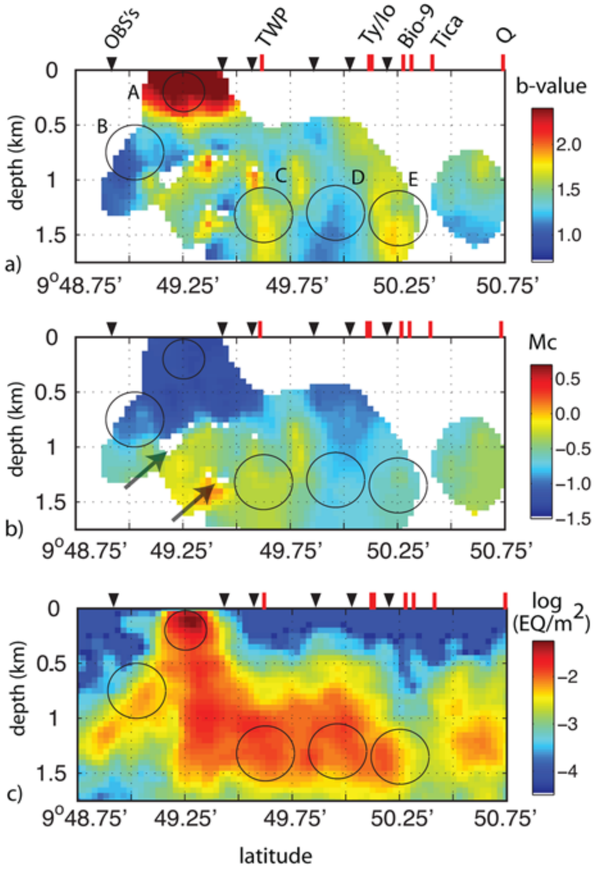

Figure 5. Axial cross sections along line A-A′ (Figure 1) showing (a) *b* value, (b) M_c value, and (c) data density. The *b* and M_c values were determined using a 3-D search radius and constant event number binning with $N = 300$. Regions of low data density have been masked out. Arrows in Figure 5b highlight an additional zone where the data have been masked due to the locally poor (>10%) fit to a power law model. Frequency magnitude plots for earthquakes within the fixed volume regions A-E are shown in Figure 6.

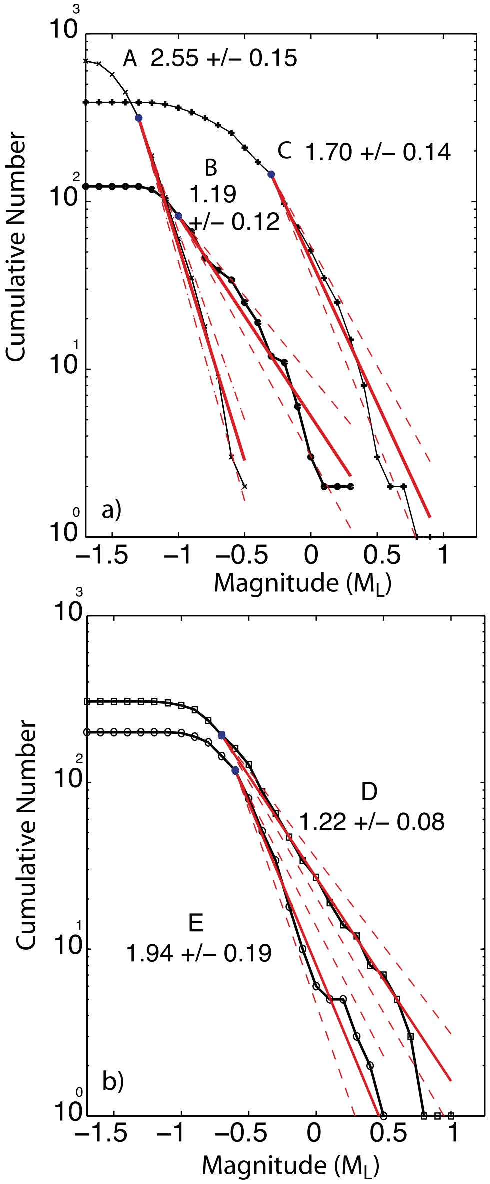

Figure 6. FMDs for regions A-E shown in the along-axis cross section (Figure 5); sampling volumes are spheres with fixed radii. Solid red lines indicate maximum likelihood fit to the data, with 1-σ limits (dashed lines). M_c values are identified by solid blue dots. See Table 2.

modeling by *Tolstoy et al.* [2008] has shown that the pattern of P and S phase arrivals is consistent with that predicted for a subvertical pipe and that this clustering of small magnitude events at shallow depth does not represent a systematic mislocation. Moreover, these data are described well by a power law FMD, with no indication of enrichment at the high or low magnitude ranges (Figure 6a).

[26] As for the completeness level within the array, at shallow depths the M_c values are the lowest (<-1) in the vicinity of the instrument triad formed near 9°49.25′N by stations 1, 2, and 3 (Figure 5b). At the deeper levels, the M_c values are lowest near the center of the array, 9°50′N, and increase near the margins of the array. Some grid nodes near the convergence of the downflow zone and the main hydrothermal cell (~9°49′N) return best fitting R values >10% for data ranges $\geq$0.7 magnitude units. The comparably poor fit of these nodes to the power law model may indicate a finer-scale spatial heterogeneity or a localized temporal shift in *b* value. These regions have been masked in Figures 5a and 5b.

[27] For events occurring outside of the array, the hypocentral depth is not sufficiently constrained to generate a cross-sectional view. Therefore, a map view is created using constant event number bins that are defined based only on the epicentral (x−y) distance to each node (Figure 7). To better compare events within and outside of the array, the high *b* value activity within the shallow down flow zone is excluded from this analysis. These downflow zone earthquakes are of extremely small magnitude ($M_L < -0.5$) and would not be detected if they occurred external to the array.

[28] In map view the *b* value pattern within the array shows heterogeneity at scales comparable to that observed in cross section, with significant differences between patches of high and low *b* value (Figures 7 and 8). The lowest *b* values are observed to the northeast of the array, with these

Table 2. Probability (p) Values for Fixed-Volume Cross-Sectional Regions[a]

	M_c	N	b	B	C	D	E
A	−1.3	315	2.55	1.5×10^{-10}	1.9×10^{-4}	8.7×10^{-16}	1.3×10^{-2}
B	−1.0	82	1.19	–	7.5×10^{-3}	3.6×10^{-1}	1.0×10^{-3}
C	−0.3	145	1.74		–	2.3×10^{-3}	2.5×10^{-1}
D	−0.7	192	1.22			–	2.0×10^{-4}
E	−0.6	118	1.94				–

[a] Determined using equation (6) [*Utsu*, 1992].

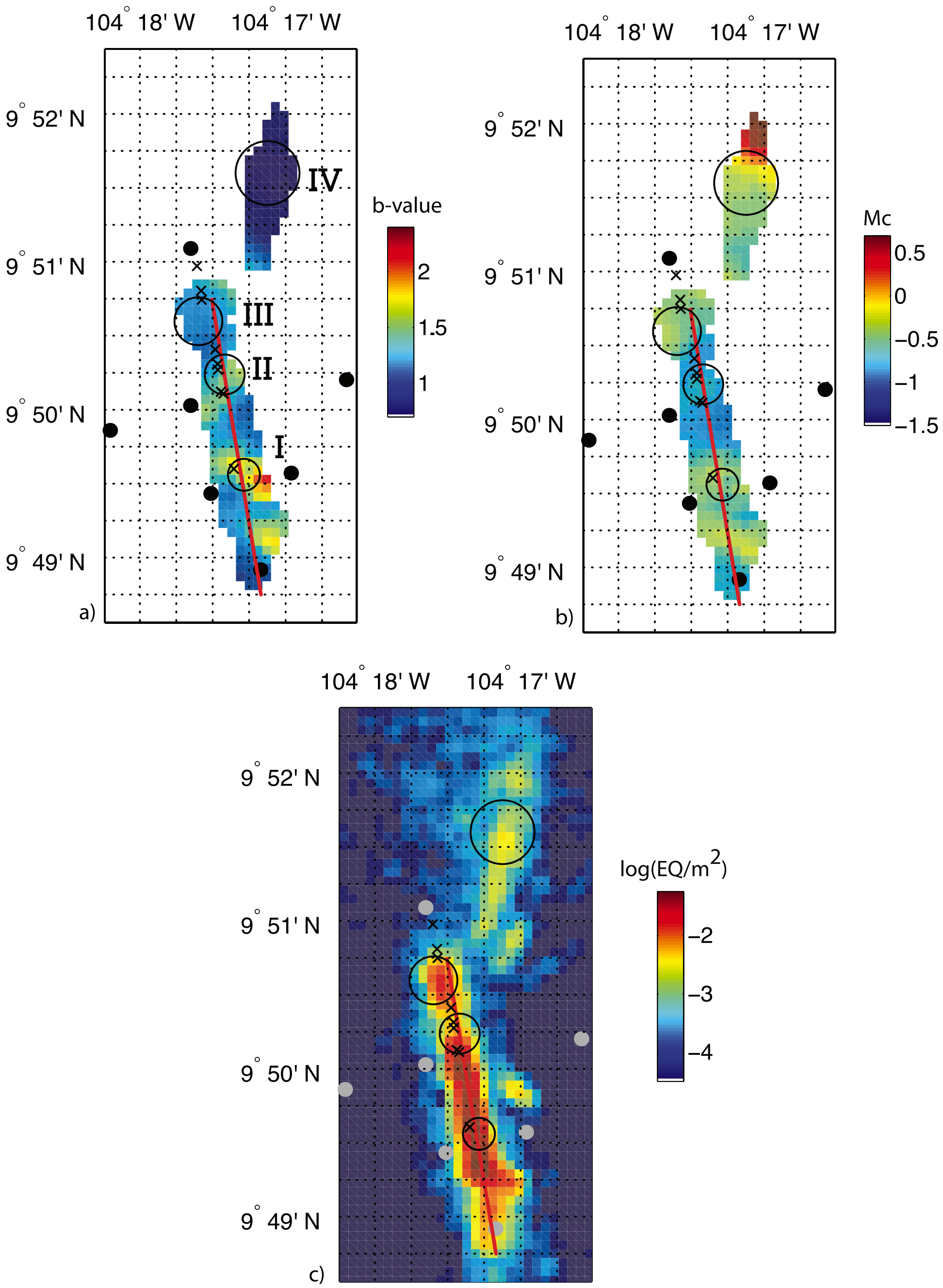

Figure 7. Map view representation of (a) *b* value, (b) M_c value, and (c) data density. The *b* and M_c values were determined using a 2-D horizontal search radius and constant event number binning with $N = 300$. Data from the shallow down flow zone (depth < 0.65 km) have been excluded for this analysis. Frequency-magnitude plots for earthquakes within the fixed volume regions I-IV are shown in Figure 8. Large dots show OBS locations and crosses denote the locations of the high-temperature vent sites labeled in Figure 1.

values being significantly different relative to the intraarray values (Figure 8; Table 3). The maximum earthquake magnitude also increases within this north-northeast trending band (Figure 8), which lies just off axis, trending between roughly 0.5 and 1 km to the east of the AST (Figure 1).

[29] Assessing magnitude-dependent bias in the location of events outside of the array is difficult; however, we note that events to the northeast of the array are well described by a power law FMD (Figure 8), with the M_c value increasing systematically away from the array (Figure 7b).

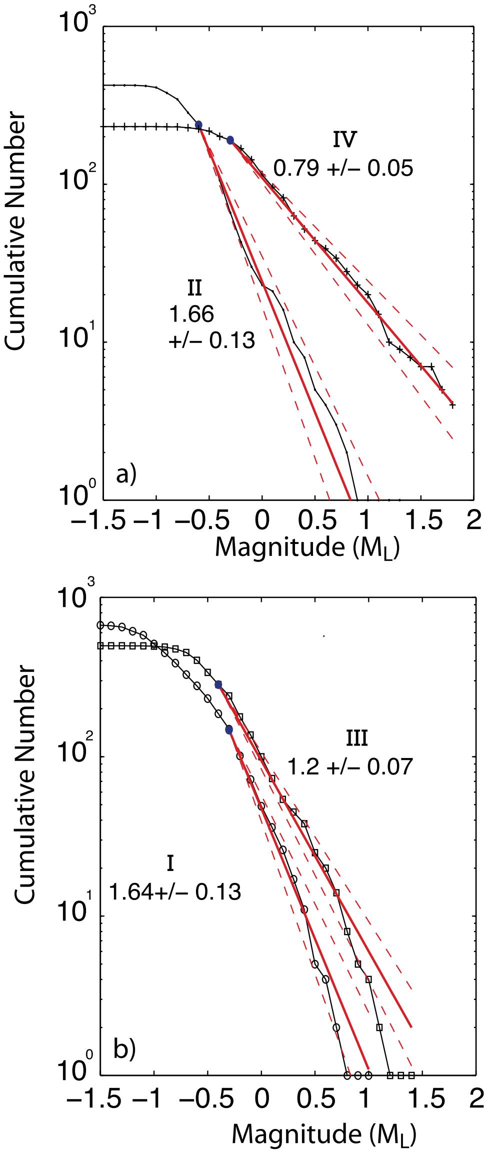

Figure 8. FMDs for the regions I-IV shown in map view (Figure 7); sampling volumes are vertically oriented cylinders with fixed radii. Solid red lines indicate maximum likelihood fit to the data, with 1-sigma limits (dashed lines). M_c values are identified by solid blue dots. See Table 3.

5.2. Spatiotemporal Patterns

[30] The spatial patterns described in section 5.1 represent temporal averages during the period October 2003 through April 2004. To examine the stability of these *b* value patterns, the data are divided into three temporal subsets containing equal numbers of events and overlapping by 50%. The parameters *b* and M_c are then calculated within each subset using constant event number bins with $N = 150$. The *b* value results shown in Figure 9 indicate that the general patterns in the larger data set are sustained within each observational window, including a region of $b \geq 2$ within the shallow down flow zone and smaller-amplitude highs near the center of the circulation cell (9°49.6′N) and beneath the high-temperature upflow zone (9°50.25′N). These observations indicate that enhanced fracture density and/or higher pore pressures are maintained within these zones. However, the axial cross sections do not reveal a laterally continuous region of high *b* value (high pore pressure or heterogeneous structure) connecting the upflow and downflow zones, implying that flow paths through the reservoir should not be viewed as pipe-like.

[31] One area of notable *b* value change occurs within the northernmost region of the array, which is separated from the southern cell by a gap in seismicity near 9°50.35′N. This region's pronounced decrease in the *b* value through time is explored in more detail in Figure 10. Although data density limits the temporal resolution, a shift in *b* value can be constrained (using $N = 110$) to occur sometime during the month of February 2004. Temporal decreases in *b* value indicate increasing stress conditions or potentially a reorganization of the fracture network within this volume. The former scenario could be driven by a reduction in pore fluid pressure accompanying the escape of fluids trapped within the region. If the upflow time for these fluids is short and their temperature is anomalous a correlated change in fluid exit temperature might be expected at the vents [e.g., *Sohn et al.*, 1998, 1999]. However, there are no dramatic or widespread changes correlated with this local drop in *b* value (Figure 10c), only a long-term temperature drop of ~4°C at Biovent beginning in February 2004.

[32] Although most of the instrumented high temperature sites exhibit stable fluid exit temperatures throughout the deployment, two of the five records from the Bio 9 vent complex show variability during the period November 2003 through January

Table 3. Probability (*p*) Values for Fixed Volume Map View Regions[a]

	M_c	N	b	II	III	IV
I	−0.3	147	1.64	3.6×10^{-1}	4.7×10^{-3}	2.8×10^{-10}
II	−0.6	238	1.66	–	6.4×10^{-4}	7.1×10^{-14}
III	−0.4	248	1.20		–	2.7×10^{-5}
IV	−0.3	190	0.79			–

[a] Determined using equation (6) [*Utsu*, 1992].

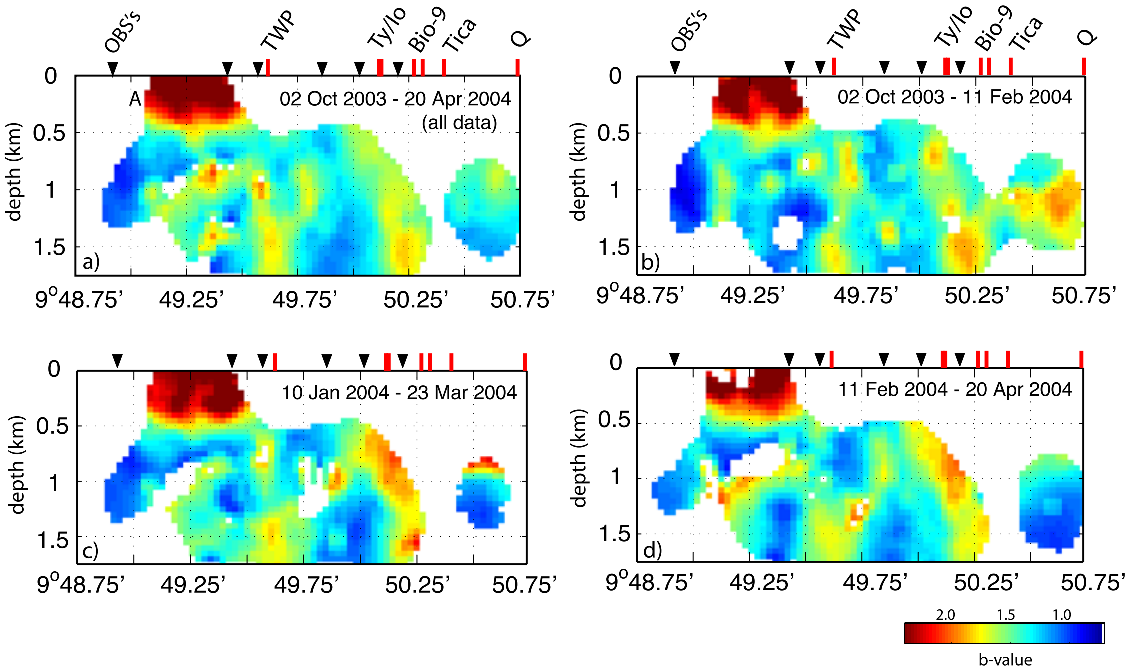

Figure 9. Axial cross sections showing *b* value during different time windows (a) 2 October 2003 to 20 April 2004 (entire data set); (b) 2 October 2003 to 11 February 2004; (c) 10 January 2004 to 23 March 2004; (d) 11 February 2004 to 20 April 2004. A constant number of events (N = 150) is mapped to each spatial node.

2004, including a drop of ∼10°C in early December 2003. These changes, however, are extremely localized spatially, with thermisters deployed within 10 m of these sites recording no change in temperature. This behavior requires subsurface perturbations occurring at similar spatial scales, which cannot be resolved by our *b* value gridding technique.

5.3. Robustness of *b* Value Estimates in Heterogeneous Settings

[33] In Figure 11 the *b* value is examined as a function of time for all earthquakes within the main hydrothermal cell, excluding the shallow downflow region. Constant event number nodes with N = 300 are used, with M_c selected both empirically (blue) and using a conservative fixed value of M_c −0.2 (red). The bin size is comparable to the total number of earthquakes available in most previous MOR *b* value studies (Table 1) and is large relative to the size of individual earthquake sequences (swarms or aftershocks) within this data set (Figure 3).

[34] Although the results indicate no long-term trend, consistent with the general pattern seen in Figure 10, temporal fluctuations are observed with *b* value ranging from 1.1 to 1.7. To test whether this variability in the *b* value may arise simply due to our sampling of a crustal volume with heterogeneous *b* value and M_c, the cataloged magnitudes are randomized in time and the *b* value is again estimated within a series of constant event number bins (N = 300). The results from 1000 permutations indicate that the observed range of *b* values (1.1−1.7) has a >70% probability of being met or exceeded by a series random samplings. Hence, the apparent temporal fluctuations observed cannot be attributed to physical changes within the hydrothermal system.

[35] This result demonstrates the importance of considering the stationarity of FMD data sets. Specifically, if the *b* value is determined by averaging over heterogeneous crustal volumes and/or by combining regions with spatially variable detection thresholds, the result should be interpreted cautiously. Successive samplings can be expected to return variable *b* value results depending on the distribution of hypocenters that occur during a given time window. Analogous situations have been described in terrestrial settings [e.g., *Wiemer and Wyss*, 2000, 2002].

6. Summary and Discussion

[36] This is the first study to examine microearthquake *b* value along a fast spreading ridge system

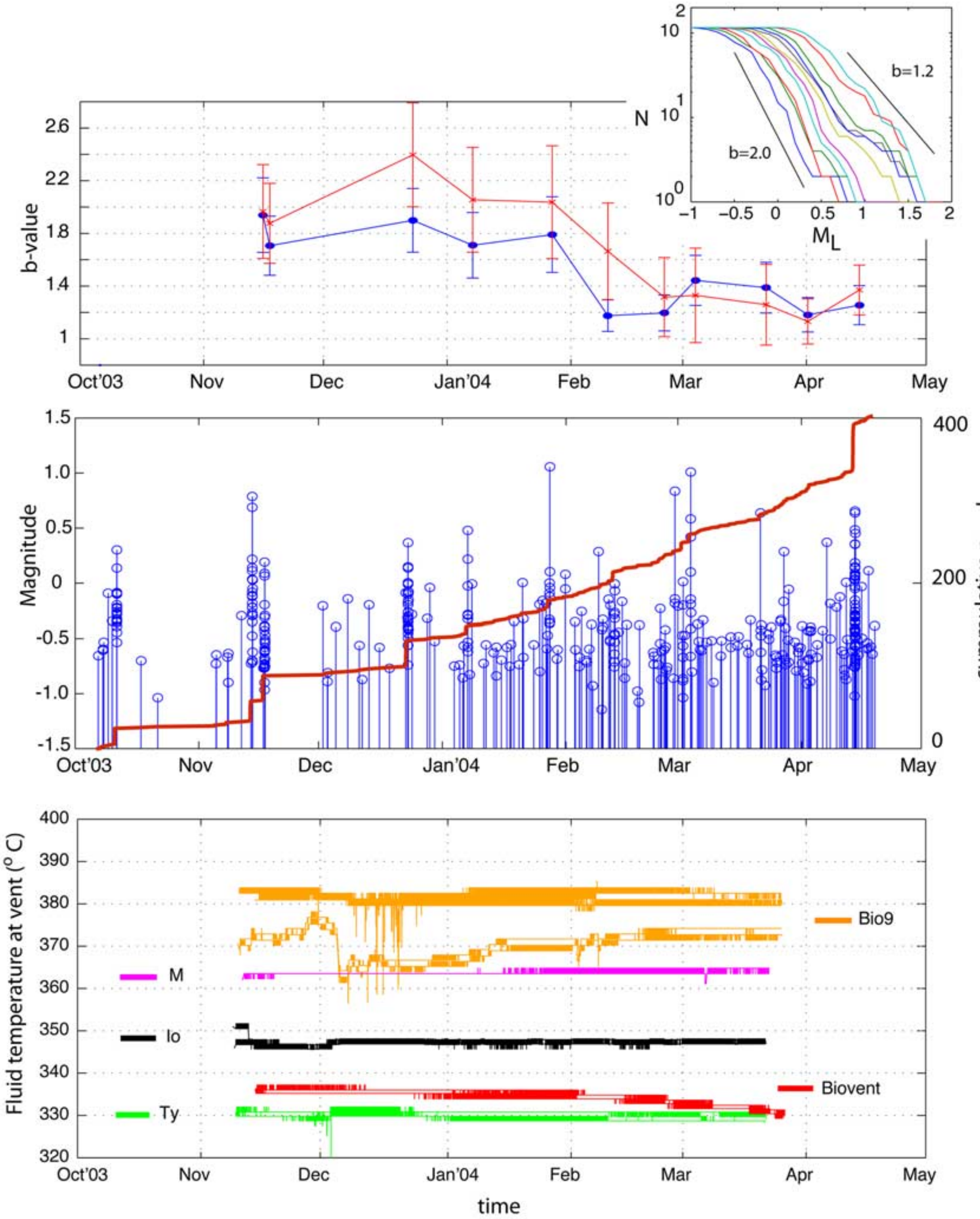

Figure 10. (a) Temporal evolution of *b* value within the northern portion of the array ($N = 110$). Events were selected within a 400 m radius spherical volume centered on axis (9°50.61N, 104°17.41W) at a depth of 1.35 km. Red curve shows *b* value calculated using a conservative M_c value of M_L −0.2. Inset shows FMD at each temporal node, with successive curves offset in magnitude for clarity. Note the somewhat bimodal appearance of the data during the transition time, as these nodes sample data from both the high and low *b* value populations. (b) Time-magnitude distribution of events considered (blue) and cumulative number through time (red). (c) Temperature records from hydrothermal sites within the 9°50′N vent field. See locations within Figures 1 and 2.

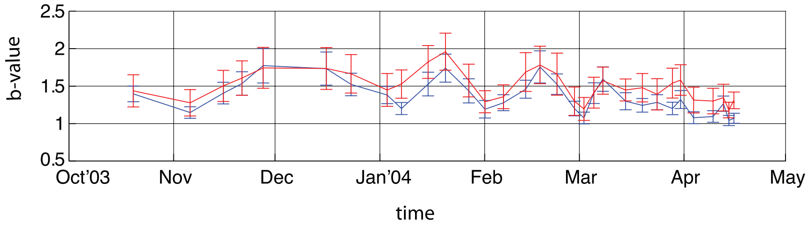

Figure 11. Microearthquake *b* value as a function of time for events within the main hydrothermal cell (9°48.75–50.75′N, depth > 0.65 km). Red lines indicate estimates of *b* value calculated using a M_c value fixed at $M_L = -0.2$. The results compare well with estimates obtained by fitting M_c and *b* simultaneously, where M_c was determined empirically to range between −0.3 and −0.8 within this zone. Data are binned with $N = 300$ and 50% overlap between temporal nodes. No long-term trend is observed, and the apparent temporal fluctuations may be related to sampling a crustal volume with heterogeneous *b* and M_c values, rather than physical changes within the hydrothermal cell. See section 5.3 for discussion.

and the first investigation of 3-D spatial and temporal *b* value patterns along any oceanic spreading center. These analyses are possible due to the long duration of this microearthquake catalog relative to previous OBS studies (Table 1), careful analyst review of phase arrival data and the determination of precise locations for a large number of densely distributed seismic events.

[37] MOR seismicity commonly has been interpreted as "magmatic" or "tectonic" based on the absolute value of the FMD's scaling exponent, with larger *b* value taken to indicate seismic activity driven by magmatic processes [e.g., *Tolstoy et al.*, 2001]. However, during the October 2003 through April 2004 period of observation, the highest *b* values (>2) are observed in the downflow zone identified by *Tolstoy et al.* [2008]. This is the region where cold seawater is being entrained within the crust, and the larger relative proportion of small versus large earthquakes cannot be linked directly to the process of intrusion. Rather, high *b* values at shallow depths are consistent with the low deviatoric stress levels and the structurally heterogeneous nature of the uppermost oceanic crust, which is formed by the extrusion of lava and the repeated emplacement of sheeted dikes [*Fornari et al.*, 2004]. This portion of the crust is known to exhibit low seismic velocities, linked to its highly fractured and permeable character [e.g., *Sohn et al.*, 2004].

[38] The parameter b decreases with depth, reaching an average value of ~1.4 within the main hydrothermal cell. This is consistent with decreasing structural heterogeneity and/or increasing ambient stress levels due to the greater overburden pressures at depth. On land, decreasing *b* values with depth have been reported in both volcanic and nonvolcanic settings, where they have been linked to similar processes [e.g., *Gerstenberger et al.*, 2001; *Wyss et al.*, 2008]. This pattern, however, is not universal in terrestrial settings and future investigations will be needed to determine if high *b* values are broadly characteristic of the shallowest ocean crust. Alternatively, enhanced structural heterogeneity, favoring higher *b* values, may be linked to the presence of the segment B1/B2 boundary within the downflow zone [*Haymon et al.*, 1991; *Wright et al.*, 1995]; however, the low density of hypocenters outside of the downflow zone does not allow this hypothesis to be tested within the 9°50′N area.

[39] Although the average *b* value within the main 9°50′N hydrothermal cell is similar to that reported beneath vent fields on the intermediate spreading rate Juan de Fuca Ridge [*Golden et al.*, 2003; *Wilcock et al.*, 2002], our results suggest that studies focusing on relative changes in the *b* value may provide more detailed information on subsurface fracture distributions and/or stress conditions. Moreover, resampling analysis shows that *b* value estimates averaged at the segment or vent field scales (e.g., Table 1) may not be good proxies for the physical conditions within the crust. In setting where the FMD or detection capabilities exhibit significant spatial heterogeneity, such estimates can be expected to return variable results depending on the distribution of hypocenters during the period of sampling.

[40] A model where *b* values are controlled primarily by thermal gradients [*Warren and Latham*, 1970] would favor an increase in *b* value approaching the AMC, which is not observed. Rather, alternating pockets of high and low *b* value are observed along the axis of the spreading center. This is interpreted to reflect some combination of changing structural heterogeneity or fluctuations in pore pressure with-

in the hydrothermal reservoir. The lowest *b* values (<1) are found on the near-axis flanks away from the well-documented hydrothermal cell between 9°49′ and 9°51′N. This is consistent with a lowering of pore pressure away from the axial region and potentially increased stress levels associated with the deeper hypocenters that may exist within slightly older crust.

[41] Temporal increases in *b* value have been noted beneath terrestrial volcanoes in association with intrusion events [e.g., *Wyss et al.*, 1997; *Wiemer et al.*, 1998]. These changes are often step like in nature and interpreted to reflect an increase in crack density in the rock volume surrounding the intrusion or an increase in pore pressure resulting from the exsolution of volatiles as the magma moves upward within the crust. Notably, during a 7-month period of increasing seismicity rate some 2 years preeruption, a broad pattern of increasing *b* value is not observed adjacent to the AMC. It is possible that the relatively volatile poor nature of MOR magmas does not promote such behavior or that eruptions in the fast spreading environment are initiated as tectonic stresses build with the upper crust, rather than in response to the influx of new magma and the development of an overpressure within the chamber. Future *b* value monitoring will be needed to establish if MOR magmatic systems produce a response similar to terrestrial volcanoes and, if so, on what timescales.

[42] Throughout most of the study area a similar spatial pattern of *b* value is sustained through time. A notable exception occurs between 9°50.4 and 50.75 N, where a localized drop in *b* value is observed in February 2004. This area is delineated by a small seismic gap (Figure 2), with both seismicity patterns and vent fluid chemistry suggesting that the region represents the southern edge of the hydrothermal cell operating to the north [*Tolstoy et al.*, 2008]. A drop in *b* value within this region could indicate a reduction in pore pressure accompanying the escape of once trapped fluids from the crustal volume. Although earthquake-induced fluid release events have been proposed previously as a mechanism for rapidly changing in vent fluid temperatures [*Sohn et al.*, 1998, 1999], no such response is observed at the instrumented high-temperature sites during this period.

[43] The hypocentral data analyzed in this study are available via the RIDGE 2000 program's data portal (http://www.ridge2000.org). In many statistical applications it will be necessary to account for variability in the detection capabilities of this array. The empirically derived magnitude-of-completeness (M_c) estimates that are produced as a byproduct of the *b* value mapping provide such information (Figures 4b, 5b, and 7b).

Appendix A: Derivation of a Local Magnitude Scale

[44] A local magnitude (M_L) scale is derived using the peak displacement amplitude measured on the vertical-channel seismometer. Following the general magnitude formulation originated by *Richter* [1935, 1958], we define:

$$M_L = \log_{10} A - \log_{10} A_o - S, \qquad \text{(A1)}$$

where A is the peak displacement in microns of the largest arriving phase, $\log_{10} A_o$ is a distance-dependent attenuation correction, and S is a station correction term. Displacement measurements are derived from the integration of the L22 velocity data. The peak is selected within a 2.25 s window after the initial P arrival. This time window captures the S phase arrival but is too short to include the water column multiple.

[45] The attenuation term ($\log_{10} A_o$) depends on scattering, anelastic attenuation, and geometric spreading along the hypocenter-to-station path. We assume a parametric form following *Bakun and Joyner* [1984].

$$-\log_{10} A_o = n \log_{10}\left(\frac{R}{R_{ref}}\right) + k\left(R - R_{ref}\right) + M^*\left(R_{ref}\right), \qquad \text{(A2)}$$

where R is the hypocentral event-to-station distance in km, the terms n and k describe the site-dependent attenuation, R_{ref} is an arbitrary reference distance taken to be 1.5 km in this study, and $M^*(R_{ref})$ is a constant which transforms the magnitude scale. $M^*(R_{ref}) = 1.4$ is adopted here, shifting the magnitude scale into approximate agreement with moment magnitude estimates and the M_w scales implemented in previous studies [e.g., *Sohn et al.*, 1998]. As activity in this area went undetected by the equatorial Pacific hydrophone array [*Fox et al.*, 2001], the equivalent body wave magnitudes of the largest events are known to be less than ∼2.5 [*Bohnenstiehl et al.*, 2002].

[46] Combining equations (A1) and (A2), the following system of equations is generated:

$$\log_{10}A_{ij} = n\log_{10}\left(\frac{R_{ij}}{R_{ref}}\right) + k\left(R_{ij} - R_{ref}\right) + \sum_{a=1}^{N_{sta}} S_a\delta_{aj} + \sum_{b=1}^{N_{event}} M_b\delta_{bi}, \tag{A3}$$

where i and j are the event and station indices, S_a is the station correction, M_b is the earthquake's local magnitude, and δ is the Krondeker delta function, equal to 1 when the indexes are equal, otherwise zero. This can be rewritten in matrix form $Gm = d$, where G consists of the R terms and the "dummy" variables prescribed by the Krondeker delta function, m contains the terms to be solved (n, k, S_a, M_b), and d holds the amplitude measurements for each arrival.

[47] Magnitude estimates are derived from arrivals at stations 002, 003, 007, and 009. Station 005 returned only hydroacoustic data, and initial analysis showed that stations 001 and 004 would not only require large station corrections but also that their station magnitudes were highly variable relative to the rest of the network. These inconsistencies presumably reflect the positioning and coupling of these freefall deployed instruments on the seafloor. To determine the parameters n, k, and S_a, only events that produced arrivals with SNR > 4 at all four stations (002, 003, 007, and 009) were used in the inversion. This produced a set of 6800 arrivals with a median station-to-event distance of 2.2 km. Errors for n, k, and S_a were estimated based on 1000 bootstrap samples of this population. The results indicate:

$$-\log_{10}A_o = 1.402(\pm 0.025)\log_{10}\left(\frac{R}{1.5}\right) + 0.094(\pm 0.007)(R - 1.5), \tag{A4}$$

with station corrections of −0.079 (±0.003), 0.162 (±0.005), −0.178 (±0.003), and 0.0.095(±0.006) at stations 002, 003, 007, and 009, respectively. This distance−dependent attenuation formula and these station corrections were then applied to all amplitude measurements recorded at stations 002, 003, 007, or 009 and having SNR > 2. Final station residuals are normally distributed with standard deviations ranging 0.13–0.15 magnitude units.

Acknowledgments

[48] We thank R.T. Weekly for his skilled efforts in reviewing phase arrival data. W.Y. Kim and M. Gold kindly assisted in setting up the seismic database and refining the detection procedures. Reviews by R. Haymon, S. White, and C. Fox significantly improved the quality and focus of the manuscript. Instrumentation provided by the National Science Foundation's (NSF) Ocean Bottom Instrument Pool (www.obsip.org). We thank the Captain, crew, and science parties of the R/V *Keldysh* and the R/V *Atlantis*. This seismic catalog was produced by funding from NSF OCE-0327283, as part of the RIDGE 2000 Program's Integrated Study Site initiative.

References

Aki, K. (1965), Maximum likelihood estimate of b in the formula log n = a−bm and its confidence limits, *Bull. Earthquake Res. Inst. Tokyo*, *43*, 237–239.

Amitrano, D. (2003), Brittle-ductile transition and associated seismicity; experimental and numerical studies and relationship with the b value, *J. Geophys. Res.*, *108*(B1), 2044, doi:10.1029/2001JB000680.

Bakun, W. H., and W. B. Joyner (1984), The M_L scale in central California, *Bull. Seismol. Soc. Am.*, *74*, 1827–1843.

Barclay, A. H., D. R. Toomey, and S. C. Solomon (2001), Microearthquake characteristics and crustal $V_p - V_s$ structure at the Mid-Atlantic Ridge, 35°N, *J. Geophys. Res.*, *106*, 2017–2034, doi:10.1029/2000JB900371.

Barton, D. J., G. R. Foulger, J. R. Henderson, and B. R. Julian (1999), Frequency-magnitude statistics and spatial correlation dimensions of earthquakes at Long Valley Caldera, California, *Geophys. J. Int.*, *138*, 563–570, doi:10.1046/j.1365-246X.1999.00898.x.

Bird, P., Y. Y. Kagan, and D. D. Jackson (2002), Plate tectonics and earthquake potential of spreading ridges and oceanic transform faults, in *Plate Boundary Zones*, *Geodyn. Ser.*, vol. 30, edited by S. Stein and J. T. Freymueller, pp. 203–218, AGU, Washington, D. C.

Bohnenstiehl, D. R., and R. P. Dziak (2008), Mid-ocean ridge seismicity, in *Encyclopedia of Ocean Sciences*, edited by J. H. Steele et al., Academic, London.

Bohnenstiehl, D. R., M. Tolstoy, R. P. Dziak, C. G. Fox, and D. K. Smith (2002), Aftershock sequences in the mid-ocean ridge environment: An analysis using hydroacoustic data, *Tectonophysics*, *354*, 49–70, doi:10.1016/S0040-1951(02)00289-5.

Bohnenstiehl, D. R., R. P. Dziak, M. Tolstoy, C. G. Fox, and M. Fowler (2004), Temporal and spatial history of the 1999–2000 Endeavour Segment seismic series, Juan de Fuca Ridge, *Geochem. Geophys. Geosyst.*, *5*, Q09003, doi:10.1029/2004GC000735.

Carbotte, S. M. (2001), Mid-ocean ridge seismic structure, in *Encyclopedia of Ocean Sciences*, edited by J. H. Steele et al., pp. 1788–1798, Academic, London.

Cessaro, R. K., and D. M. Hussong (1986), Transform seismicity at the intersection of the Oceanographer fracture zone and the Mid-Atlantic Ridge, *J. Geophys. Res.*, *91*, 4839–4853, doi:10.1029/JB091iB05p04839.

Dieterich, J., V. Cayol, and P. G. Okubo (2000), The use of earthquake rate changes as a stress meter at Kilauea Volcano, *Nature*, *408*, 457–460, doi:10.1038/35044054.

Escartin, J., S. A. Soule, D. J. Fornari, M. A. Tivey, H. Schouten, and M. R. Perfit (2007), Interplay between faults and lava flows in construction of the upper oceanic crust: The East Pacific Rise crest 9°25′–9°58′N, *Geochem. Geophys. Geosyst.*, *8*, Q06005, doi:10.1029/2006GC001399.

Fornari, D. J., R. M. Haymon, M. R. Perfit, T. K. P. Gregg, and M. H. Edwards (1998), Axial summit trough of the East Pacific Rise 9°–10°N; geological characteristics and evolution of the axial zone on fast spreading mid-ocean ridges, *J. Geophys. Res.*, *103*, 9827–9855, doi:10.1029/98JB00028.

Fornari, D. J., et al. (2004), Submarine lava flow emplacement at the East Pacific Rise 9°50′N: Implications for uppermost ocean crust stratigraphy and hydrothermal fluid circulation, in *Mid-Ocean Ridges: Hydrothermal Interactions Between the Lithosphere and Oceans*, *Geophys. Monogr. Ser.*, vol. 148, edited by C. R. German, J. Lin, and L. M. Parson, pp. 187–217, AGU, Washington, D. C.

Fox, C. G., R. P. Dziak, H. Matsumoto, and A. E. Schreiner (1994), Potential for monitoring low-level seismicity on the Juan de Fuca Ridge using military hydrophone array, *Mar. Technol. Soc. J.*, *27*, 22–30.

Fox, C. G., H. Matsumoto, and T.-K. A. Lau (2001), Monitoring Pacific Ocean seismicity from an autonomous hydrophone array, *J. Geophys. Res.*, *106*, 4183–4206, doi:10.1029/2000JB900404.

Francis, T. J. G. (1968), The detailed seismicity of mid-oceanic ridges, *Earth Planet. Sci. Lett.*, *4*, 39–46, doi:10.1016/0012-821X(68)90051-4.

Frohlich, C., and S. D. Davis (1993), Teleseismic b values; or, much ado about 1.0, *J. Geophys. Res.*, *98*, 631–644, doi:10.1029/92JB01891.

Gerstenberger, M., S. Wiemer, and D. Giardini (2001), A systematic test of the hypothesis that the b value varies with depth in California, *Geophys. Res. Lett.*, *28*, 57–60, doi:10.1029/2000GL012026.

Golden, C. E., S. C. Webb, and R. A. Sohn (2003), Hydrothermal microearthquake swarms beneath active vents at Middle Valley, northern Juan de Fuca Ridge, *J. Geophys. Res.*, *108*(A1), 2027, doi:10.1029/2001JB000226.

Gutenberg, B., and C. F. Richter (1944), Frequency of earthquakes in California, *Bull. Seismol. Soc. Am.*, *34*, 185–188.

Haymon, R. M. (1996), The response of ridge crest hydrothermal systems to segmented, episodic magma supply, in *Tectonic, Magmatic, Hydrothermal, and Biological Segmentation of Mid-Ocean Ridges*, edited by C. J. MacLeod, P. A. Tyler and C. L. Walker, *Geol. Soc. London Spec. Publ.*, 118, 157–168.

Haymon, R. M., D. J. Fornari, M. H. Edwards, S. Carbotte, D. Wright, and K. C. Macdonald (1991), Hydrothermal vent distribution along the East Pacific Rise crest (9°09′–54′N) and its relationship to magmatic and tectonic processes on fast-spreading mid-ocean ridges, *Earth Planet. Sci. Lett.*, *104*, 513–534, doi:10.1016/0012-821X(91)90226-8.

Haymon, R. M., et al. (1993), Volcanic eruption of the mid-ocean ridge along the East Pacific Rise crest at 9° 45–52′N: Direct submersible observations of seafloor phenomena associated with an eruption event in April, 1991, *Earth Planet. Sci. Lett.*, *119*, 85–101, doi:10.1016/0012-821X(93)90008-W.

Henderson, J. R., D. J. Barton, and G. R. Foulger (1999), Fractal clustering of induced seismicity in The Geysers geothermal area, California, *Geophys. J. Int.*, *139*, 317–324, doi:10.1046/j.1365-246x.1999.00939.x.

Kagan, Y. Y. (2002), Seismic moment distribution revisted: I. Statistical results, *Geophys. J. Int.*, *148*, 520–541, doi:10.1046/j.1365-246x.2002.01594.x.

Katsumata, K., T. S. Sato, J. Kasahara, N. Hirata, R. Hino, N. Takahashi, M. Sekine, S. Miura, S. Koresawa, and N. Wada (2001), Microearthquake seismicity and focal mechanisms at the Rodriguez Triple Junction in the Indian Ocean using ocean bottom seismometers, *J. Geophys. Res.*, *106*, 30,689–30,699, doi:10.1029/2000JB000106.

Kent, G. M., A. J. Harding, and J. A. Orcutt (1993), Distribution of magma beneath the East Pacific Rise between the Clipperton Transform and the 9°17′N Deval from forward modeling of common depth point data, *J. Geophys. Res.*, *98*, 13,945–13,969, doi:10.1029/93JB00705.

Kissling, E., W. L. Ellsworth, D. Eberhart-Phillips, and U. Kradolfer (1994), Initial reference model in local earthquake tomography, *J. Geophys. Res.*, *99*, 19,635–19,646, doi:10.1029/93JB03138.

Klein, F. W. (2002), User's guide to HYPOINVERSE-2000, a Fortran program to solve for earthquake locations and magnitudes, *U. S. Geol. Surv. Open File Rep. 02-171*, 123 pp.

Kong, L. S. L., S. C. Solomon, and G. M. Purdy (1992), Microearthquake characteristics of a mid-ocean ridge along-axis high, *J. Geophys. Res.*, *97*, 1659–1685, doi:10.1029/91JB02566.

Lilwall, R. C., T. J. G. Francis, and I. T. Porter (1977), Ocean bottom seismograph observations on the Mid Atlantic Ridge at 45°N, *Geophys. J. R. Astron. Soc.*, *51*, 357–370.

Mackwell, S. J., M. E. Zimmerman, and D. L. Kohlstedt (1998), High-temperature deformation of dry diabase with application to tectonics on Venus, *J. Geophys. Res.*, *103*, 975–984, doi:10.1029/97JB02671.

Mogi, K. (1962), Fracture of rocks, *Bull. Volcanol. Soc. Jpn.*, *7*, 89–101.

Nuannin, P., O. Kulhanek, L. Persson, and K. Tillman (2002), Forecasting of increased induced seismicity in the Zinkgruvan mine Sweden, by using temporal variations of *b*-values, *Acta Montana*, *125*, 13–25.

Nuannin, P., L. Persson, and T. Askemur (2005), Inverse correlation between induced seismicity and *b*-value, observed in the Zinkruvan mine, Sweden, *Acta Geodyn. Geomat.*, *4*, 5–13.

Oncel, A. O., and M. Wyss (2000), The major asperities of the 1999 M_w = 7.4 Izmit earthquake defined by the microseismicity of the two decades before it, *Geophys. J. Int.*, *143*, 501–506, doi:10.1046/j.1365-246X.2000.00211.x.

Richter, C. F. (1935), An instrumental earthquake-magnitude scale, *Bull. Seismol. Soc. Am.*, *25*, 1–32.

Richter, C. F. (1958), *Elementary Seismology*, W. H. Freemann, San Francisco, Calif.

Scheirer, D. S., T. M. Shank, and D. J. Fornari (2006), Temperature variations at diffuse and focused flow hydrothermal vent sites along the northern East Pacific Rise, *Geochem. Geophys. Geosyst.*, *7*, Q03002, doi:10.1029/2005GC001094.

Scholz, C. H. (1968), The frequency-magnitude relation of microfracturing in rock and its relation to earthquakes, *Bull. Seismol. Soc. Am.*, *58*, 399–415.

Scholz, C. H. (2002), *The Mechanics of Earthquakes and Faulting*, 2nd ed., 471 pp., Cambridge Univ. Press, Cambridge, U. K.

Schorlemmer, D., S. Wiemer, and M. Wyss (2005), Variations in earthquake-size distribution across different stress regimes, *Nature*, *437*, 539–542, doi:10.1038/nature04094.

Shank, T. M., D. J. Fornari, K. L. Von Damm, M. D. Lilley, R. M. Haymon, and R. Lutz (1998), Temporal and spatial patterns of biological community development at nascent deep-sea hydrothermal vents (9°50′N, East Pacific Rise), *Deep Sea Res., Part II*, *45*, 465–515, doi:10.1016/S0967-0645(97)00089-1.

Shi, Y., and B. A. Bolt (1982), The standard error of the magnitude-frequency b value, *Bull. Seismol. Soc. Am.*, *72*(5), 1677–1687.

Sohn, R. A., D. J. Fornari, K. L. Von Damm, J. A. Hildebrand, and S. C. Webb (1998), Seismic and hydrothermal evidence for a cracking event on the East Pacific Rise crest at 9 degrees 50′N, *Nature*, *396*, 159–161, doi:10.1038/24146.

Sohn, R. A., J. A. Hildebrand, and S. C. Webb (1999), A microearthquake survey of the high-temperature vent fields on the volcanically active East Pacific Rise, *J. Geophys. Res.*, *104*, 25,367–25,377, doi:10.1029/1999JB900263.

Sohn, R. A., S. C. Webb, and J. A. Hildebrand (2004), Fine-scale seismic structure of the shallow volcanic crust on the East Pacific Rise at 9°50′N, *J. Geophys. Res.*, *109*, B12104, doi:10.1029/2004JB003152.

Soule, S. A., et al. (2005), Channelized lava flows at the East Pacific Rise crest, 9–10°N; the importance of off-axis lava transport in developing the architecture of young oceanic crust, *Geochem. Geophys. Geosyst.*, *6*, Q08005, doi:10.1029/2005GC000912.

Soule, S. A., et al. (2007), New insights into mid-ocean ridge volcanic processes from the 2005–2006 eruption of the East Pacific Rise, 9°46′N–9°56′N, *Geology*, *35*, 1079–1082, doi:10.1130/G23924A.1.

Stroup, D. F., D. R. Bohnenstiehl, M. Tolstoy, F. Waldhauser, and R. T. Weekly (2007), Pulse of the seafloor: Tidal triggering of microearthquakes at 9°50′N East Pacific Rise, *Geophys. Res. Lett.*, *34*, L15301, doi:10.1029/2007GL030088.

Tilmann, F., E. Flueh, L. Planert, T. Reston, and W. Weinrebe (2004), Microearthquake seismicity of the Mid-Atlantic Ridge at 5 degrees S; a view of tectonic extension, *J. Geophys. Res.*, *109*, B06102, doi:10.1029/2003JB002827.

Tolstoy, M., D. R. Bohnenstiehl, M. Edwards, and G. Kurras (2001), Seismic character of volcanic activity at the ultraslow-spreading Gakkel Ridge, *Geology*, *29*, 1139–1142, doi:10.1130/0091-7613(2001)029<1139:SCOVAA>2.0.CO;2.

Tolstoy, M., et al. (2006), A sea-floor spreading event captured by seismometers, *Science*, *314*, 1920–1922, doi:10.1126/science.1133950.

Tolstoy, M., F. Waldhauser, D. R. Bohnenstiehl, R. T. Weekly, and W.-Y. Kim (2008), Seismic identification of along-axis hydrothermal flow on the East Pacific Rise, *Nature*, *451*, 181–184, doi:10.1038/nature06424.

Toomey, D. R., S. C. Solomon, and G. M. Purdy (1988), Microearthquakes beneath median valley of Mid-Atlantic Ridge near 23 degrees N: Tomography and tectonics, *J. Geophys. Res.*, *93*, 9093–9112.

Urbancic, T. I., C. I. Trifu, J. M. Long, and R. P. Young (1992), Space-time correlations of b values with stress release, *Pure Appl. Geophys.*, *139*, 449–462, doi:10.1007/BF00879946.

Utsu, T. (1992), On seismicity, *Rep. Jt. Res. Inst. Stat. Math.*, *34*, pp. 139–157, Inst. Stat. Math, Tokyo.

Waldhauser, F. (2001), HypoDD: A program to compute double-difference hypocenter locations, *U. S. Geol. Surv. Open File Rep.*, *01–113*, 25 pp.

Waldhauser, F., and W. L. Ellsworth (2000), A double-difference earthquake location algorithm; method and application to the northern Hayward Fault, California, *Bull. Seismol. Soc. Am.*, *90*, 1353–1368, doi:10.1785/0120000006.

Warren, N. W., and G. V. Latham (1970), An experimental study of thermally induced microfracturing and its relation to volcanic seismicity, *J. Geophys. Res.*, *75*, 4455–4464, doi:10.1029/JB075i023p04455.

Westerhaus, M., M. Wyss, R. Yilmaz, and J. Zschau (2002), Correlating variations of b values and crustal deformations during the 1990s may have pinpointed the rupture initiation of the M_w = 7.4 Izmit earthquake of 1999 August 17, *Geophys. J. Int.*, *148*, 139–152, doi:10.1046/j.0956-540x.2001.01554.x.

White, S. M., R. M. Haymon, and S. Carbotte (2006), A new view of ridge segmentation and near-axis volcanism at the East Pacific Rise, 8°–12°N, from EM300 multibeam bathymetry, *Geochem. Geophys. Geosyst.*, *7*, Q12O05, doi:10.1029/2006GC001407.

Wiemer, S., and M. Wyss (1997), Mapping the frequency-magnitude distribution in asperities; an improved technique to calculate recurrence times?, *J. Geophys. Res.*, *102*, 15,115–15,128, doi:10.1029/97JB00726.

Wiemer, S., and M. Wyss (2000), Minimum magnitude of completeness in earthquake catalogs; examples from Alaska, the western United States, and Japan, *Bull. Seismol. Soc. Am.*, *90*, 859–869, doi:10.1785/0119990114.

Wiemer, S., and M. Wyss (2002), Mapping spatial variability of the frequency-magnitude distribution of earthquakes, *Adv. Geophys.*, *45*, 259–302.

Wiemer, S., S. R. McNutt, and M. Wyss (1998), Temporal and three-dimensional spatial analyses of the frequency-magnitude distribution near Long Valley Caldera, California, *Geophys. J. Int.*, *134*, 409–421, doi:10.1046/j.1365-246x.1998.00561.x.

Wilcock, W. S. D., S. D. Archer, and G. M. Purdy (2002), Microearthquakes on the Endeavour Segment of the Juan de Fuca Ridge, *J. Geophys. Res.*, *107*(B12), 2336, doi:10.1029/2001JB000505.

Wolfe, C. J., G. M. Purdy, D. R. Toomey, and S. C. Solomon (1995), Microearthquake characteristics and crustal velocity structure at 29 degrees N on the Mid-Atlantic Ridge: The architecture of a slow spreading segment, *J. Geophys. Res.*, *100*(B12), 24,449–24,472.

Wright, D. J., R. Haymon, and D. J. Fornari (1995), Crustal fissuring and its relationship to magmatic and hydrothermal processes on the East Pacific Rise crest (9°12′ to 54′N), *J. Geophys. Res.*, *100*, 6097–6120, doi:10.1029/94JB02876.

Wyss, M. (1973), Towards a Physical Understanding of the Earthquake Frequency Distribution, *Geophys. J. R. Astron. Soc.*, *31*, 341–359.

Wyss, M., and Y. Toya (2000), Is background seismicity produced at a stationary Poissonian rate?, *Bull. Seismol. Soc. Am.*, *90*, 1174–1187, doi:10.1785/0119990158.

Wyss, M., K. Shimazaki, and S. Wiemer (1997), Mapping active magma chambers by b values beneath the off-Ito Volcano, Japan, *J. Geophys. Res.*, *102*, 20,413–420,422, doi:10.1029/97JB01074.

Wyss, M., C. G. Sammis, R. M. Naudeau, and S. Wiemer (2004), Fractal dimension and b-value on creeping and locked patches of the San Andreas Fault near Parkfield, California, *Bull. Seismol. Soc. Am.*, *94*, 410–421, doi:10.1785/0120030054.

Wyss, M., F. Pacchiani, A. Deschamps, and G. Patau (2008), Mean magnitude variations of earthquakes as a function of depth: Different crustal stress distribution depending on tectonic setting, *Geophys. Res. Lett.*, *35*, L01307, doi:10.1029/2007GL031057.